Climate-driven decoupling of wetland and upland biomass trends on the mid-Atlantic coast

Yaping Chen[1*], Matthew L. Kirwan[1]

[1]Virginia Institute of Marine Science, William & Mary, Gloucester Point, VA, USA

*To whom correspondence and material requests should be addressed (ychen@vims.edu)

Coastal ecosystems represent a disproportionately large but vulnerable global carbon sink. Sea-level driven tidal wetland degradation and upland forest mortality threaten coastal carbon pools, but responses of the broader coastal landscape to interacting facets of climate change remain poorly understood. Here, we use 36 years of satellite observations across the mid-Atlantic sea-level rise hotspot to show that climate change has actually increased the amount of carbon stored in the biomass of coastal ecosystems despite substantial aerial loss. We find that sea-level driven reductions in wetland and low-lying forest biomass were largely confined to areas less than 2 meters above sea level, whereas the otherwise warmer and wetter climate led to an increase in the biomass of adjacent upland forests. Integrated across the entire coastal landscape, climate-driven upland greening offset sea-level driven biomass losses, such that the net impact of climate change was to increase the amount of carbon stored in coastal vegetation. These results point to a fundamental decoupling between upland and wetland carbon trends that can only be understood by integrating observations across traditional ecosystem boundaries. This holistic approach may provide a template for quantifying carbon-climate feedbacks and other aspects of coastal change that extend beyond sea-level rise alone.

Summary of Comments on 36102_2_merged_figures with legend.pdf

Page: 1

Number: 1 Author: John Subject: Sticky Note Date: 10/14/2022 11:52:29 AM

Chen, Y. and Kirwan, M.L., 2022. Climate driven decoupling of upland and wetland biomass trends on the mid-Atlantic coast. *Nature Geoscience*. https://doi.org/10.1038/s41561-022-01041-x.

Climate change is driving worldwide landscape reorganization with far-reaching consequences for global carbon stocks[1,2]. For instance, amplified warming has accelerated shrubification in high latitude tundra landscapes, facilitating a biome-wide increase in productivity known as Arctic Greening[3,4]. Increasing temperature and precipitation has boosted forest densification and facilitated upslope treeline in high-mountain regions such as the Tibetan Plateau[5,6], and altered precipitation regimes in the arid sub-Saharan Africa have allowed woodlands to carpet expansive barren and sparsely-vegetated drylands[7,8]. Together, these processes have contributed to a general greening of the terrestrial biosphere[9–11], in which the amount of carbon stored in woody biomass has increased through time[12,13].

Climate change is also transforming coastal ecosystems[14–16], which are a disproportionately large, yet highly vulnerable global carbon sink[17–19]. A prominent phenomenon unique to the coastal landscape is that declining coastal sediment supplies and accelerated sea-level rise (SLR) associated with recent warming has elicited degradation of existing marshes[20,21] and mortality of adjacent forests[15]. Recent research has explored the impacts of SLR on carbon pools in marshes[22–24] and coastal forests[25,26], but how climate change interacts with SLR to modify the integrated coastal carbon sink is largely unknown[27,28]. On one hand, SLR-driven vegetation shifts may result in net losses of biomass due to wetland degradation[20,29] and forest die-off[25,26]. On the other hand, changing climate may increase biomass by extending growing seasons[30] and ameliorating salt stress via increased precipitation[31]. The net outcome of these competing processes could influence both the direction and magnitude of carbon-climate feedbacks in coastal ecosystems.

Here, we use the extensive Landsat dataset (30 m resolution) between 1984 and 2020 to quantify landscape-scale (~12,500 km^2) Normalized Difference Vegetation Index (NDVI) trends associated with vegetation shifts (Methods) along the rapidly warming mid-Atlantic coast of North America (Extended Data Figures 1-2), a SLR hotspot characterized by extensive marsh loss and forest mortality[32,33]. Our results reveal a fundamental decoupling between negative SLR impacts at low elevations and positive climate impacts at higher elevations, such that the net impact of interacting facets of climate change is an overall increase in aboveground coastal biomass.

Vegetation shifts and lowland browning

Low-lying coastal wetlands and forests are well known to be vulnerable to SLR and erosion both globally[16,29,34,35], and within the Chesapeake Bay region[20,32,33]. Consistent with those observations, we find large-scale losses of marsh (196.8 km^2) and coastal forests (238.7 km^2) in the U.S. mid-Atlantic over the past ~40 years based on our Landsat observation (Figure 1). However, in spite of erosion and submergence at low elevations, marsh and transition forest (defined as low-lying forest between marsh and upland forests where mortality due to seawater intrusion has already begun) expanded in areal extent respectively by 2% (48.4 km^2) and 5% (12.1 km^2) (Figure 2). The loss of marshes observed in 1984 (7.7%, 196.8 km^2) occurred primarily at the seaward margin and for elevations below 0.2 m, and was compensated by new marsh that formed at higher elevations (245.2 km^2) at the expense of transition forest (134.9 km^2) and forested uplands (90.7 km^2). Transition forest advanced upslope, where the replacement of forested uplands (149.9 km^2) compensated for the aerial loss of transition forest at lower elevations (139.4 km^2) (Figure 2). The average elevation of transitional forests increased (0.12 m; 0.58 ± 0.35 m in 1984 to 0.70 ± 0.41 m in 2020) more than the average elevation of marshes (0.02 m; 0.49 ± 0.44 m to 0.51 ± 0.44 m) (Figure 2), and at a rate (3.3 mm yr^{-1}) that is almost equivalent to long-term SLR trends in the region (3-6 mm yr^{-1}). These observations imply that sea level rise is driving the migration of coastal ecosystems over large spatial scales, and that over decadal timescales, coastal forests are at least as vulnerable to SLR as the marshes that occur closer to the seaward margin.

Changes in vegetation extent closely resemble patterns of landscape greening (positive trend in NDVI) and browning (negative trend in NDVI) (Figure 1), and confirm general expectations that SLR-driven land conversion leads to coastal biomass loss[25,26]. In spite of overall browning in coastal lowlands, the rate of change varies substantially across space (Figures 1-2), reflecting the wide array of processes regulating vegetation dynamics. The most drastic browning appeared at the marsh-forest transition (i.e. transition forest), where marsh transgresses inland, replacing forest that is one to two orders of magnitude higher in aboveground biomass[25,36]. In the low-relief Blackwater National Wildlife Refuge where browning is extreme, we find that the marsh-forest boundary has retreated inland by as much as ~1,100 m since 1984 (or ~30 m yr^{-1}) – the fastest upland conversion ever recorded (Figure 1b). Other hotspots of coastal browning are associated with degradation or loss of habitats, as exemplified by massive interior ponding of marsh in the Prime Hook National Wildlife Refuge (Figure 1c) or rapid land erosion along vegetated barrier islands of Virginia Coast Reserve (Figure 1d).

We estimate cumulative AGB changes from 1984 to 2020 based on NDVI trends (Methods and Extended Data Figures 3-6), and partition the results by elevation and ecosystem (Figure 3 and Extended Data Figures 1 and 7). Despite pervasive AGB loss in marshes between elevation of 0-0.7m (-0.13 Tg), we find a small amount of AGB gain (+0.05 Tg) in marshes at higher elevations (Figure 3). This observation concurs with observations and experiments that report enhanced marsh productivity under moderately increased inundation[37,38]. Conversely, transition forests consistently lose AGB along elevation although the rate slightly lowers with higher elevations (Figure 3), possibly as a result of lessened salt stress and flooding frequency further inland[25].

Overall, we find that transition forest is the dominant avenue of coastal AGB loss (-0.20 Tg), nearly three times the amount of marsh (-0.07 Tg) (Figure 3). Considering that the area of the former is merely one tenth of the latter (Figure 2), AGB loss on per unit area of transition forest (815.4 g m^{-2}) is ~27 times that of marsh (29.7 g m^{-2}). This result is striking as previous work exploring impacts of SLR on coastal carbon cycling traditionally focuses on low lying marshes and mangroves[23,29,39,40], whereas our study highlights that reduced carbon stocks in retreating upland forests may actually represent a more pronounced feedback with future warming.

Sea-level driven decoupling of upland and lowland biomass trends

As the impact of SLR is intrinsically tied to elevation[41], we examined NDVI trends with elevation to gain a general perspective on coastal response to SLR (Figure 2). Despite intricacies within individual ecosystems discussed above, we find that across the coastal landscape, NDVI trends increase rapidly with elevation and that the landscape switches from browning to greening at an elevation of ~0.7 m (Figure 2). The benefit of rising elevation to additional landscape greening progressively weakens before vanishing as elevation approaches 1.9 m above sea level, after which landscape greening becomes relatively constant (Figure 2). These patterns are consistent regardless of the inclusion of areas modified by human activities (e.g. agriculture, urbanization, silviculture that jointly impact 18.1% of all area between 0-2 m, and 34.7% between 0-5 m) (Figure 2 and Extended Data Table 1). Thus, we interpret this “turning-point” elevation around 2 m as defining the upper elevation limit for SLR impacts on coastal environments, as hinted by the extent of range shifts in marsh and transition forest along elevation gradient (Figure 2).

Previous work suggests that a variety of climatic[31,42] and sea-level driven[37,38] factors are associated with biomass change and carbon cycling in coastal ecosystems. To identify potential drivers and their relative importance (RI) in shaping the observed patterns of NDVI trend across the region, we applied a boosted regression tree model to areas free from human disturbance (Methods). Our analyses ($r = 0.71$, $P < 0.0001$) indicate that the spatial variation in NDVI trend is mainly explained by variables broadly related to SLR (RI of 63%, 3 variables: elevation, flooding frequency, and topographic slope) and to a lesser degree by climate change (RI of 37%, 3 variables: change of annual precipitation, change of growing degree day, and maximum summer temperature) (Figure 4).

Partial-dependency plots attest that the impact of SLR is largely constrained within 2 m above sea level (Figure 4b). Relative SLR rates in the mid-Atlantic are 2-3X faster than the global average[43], and excessive inundation is recognized as a primary driver of marsh loss and tree mortality[20,26,33,38,44]. Consistent with this paradigm, we find that NDVI trend declines with increasing flooding frequency and decreasing topographic slope (Figure 4c-d), suggesting that SLR underlies the escalated browning in coastal lowlands.

Meanwhile, observed temperature (annual mean +0.8 ºC) and precipitation (annual total +140 mm) have significantly increased across the mid-Atlantic (Extended Data Figure 2). Studies from a wealth of coastal and terrestrial ecosystems have linked climate change, especially warming and wetting, with strengthened plant productivity and biomass carbon pools[9,31,45,46]. Our analyses indicate that increases in temperature and precipitation enhance regional greening, as NDVI trend rises nearly linearly with elevated precipitation and prolonged growing degree days (Figure 4e-f). Therefore, interactive components of climate change potentially lead to simultaneous and contrasting responses in coastal ecosystem, where greening of uplands is associated with direct climate impacts and browning of lowlands is associated with climate-driven SLR.

Direct and indirect climate impacts on the coastal biomass carbon sink

Interacting facets of climate change are well known to dictate carbon cycling in a range of terrestrial ecosystems[46,47], whereas in coastal ecosystems carbon cycling is largely viewed through the lens of SLR alone[48]. Although direct climate impacts are important controls on wetland productivity and carbon balance[31,39], it is unclear how the combined forces of SLR and climate change drive regional-scale carbon cycling, especially in the upland component of the coastal landscape. Our results illustrate that with increasing elevation, browning diminishes in marsh and transition forests, and that greening intensifies in adjacent upland forests, signaling a transition from SLR-driven browning to climate-driven greening (Figures 2a and 3a). Forest greening is consistent at elevations greater than 1.9 m above sea level – the aforementioned turning-point demarcating the potential limit of SLR impacts (Figure 2a), leading to a large net increase in AGB for the coastal zone as a whole (+3.76 Tg for elevations 0-5 m) (Figure 3b).

Interestingly, we also find that forest greening (+1.28 Tg) compensates for marsh and transition forest browning (-0.3 Tg), even when restricted to portions of the landscape that are negatively impacted by SLR (+1.0 Tg for elevations 0-1.9 m) (Figure 3b). These results are generally in line with recent global-scale, coarse-resolution (≥4 km pixels) satellite observations that suggest an overall enhancement of net primary production[9,49] and leaf area index[10,11] both globally and in the mid-Atlantic. However, by linking broad-scale biomass change with fine-scale vegetation shifts, we uncover substantial spatial heterogeneity – specifically the remarkable browning of coastal lowlands that would be obscured at coarser resolution.

Our analysis of aboveground biomass trends does not include changes in belowground biomass or soil carbon pools that are hard to quantify and respond to climate change in complex ways. For example, marshes contain a disproportionate amount of carbon in soils[25,50], and regional soil carbon accumulation rates can either increase or decrease as marshes become more inundated[22,51]. Therefore, our finding that climate factors have compensated for sea-level driven losses in aboveground biomass may neglect other important components of the coastal carbon budget. Similarly, our finding of functional compensation in aboveground biomass may not apply to other ecosystem functions that depend fundamentally on ecosystem size and location. For instance, sea-level rise is leading to the loss of freshwater forested wetlands that are themselves highly valued for habitat provision, water quality improvement, and flood protection[52,53].

Nevertheless, our finding that climate-driven upland greening has compensated for lowland browning largely contrasts previous work that generally emphasizes sea-level driven losses of biomass within marshes and coastal forests[25,26]. Thus, our work indicates that the combined influences of global change have been to increase the size of the coastal biomass carbon sink (Figure 3), even in a region that is a hotspot for accelerated sea-level rise, marsh degradation, and forest mortality[32,33,43]. This unique decoupling between SLR-driven wetland browning and climate-driven upland greening illustrates the need to quantify carbon dynamics across traditional ecosystem boundaries that respond differently to interacting factors of global change.

Acknowledgements. Primary funding for this work comes from the National Science Foundation (#1654374, MLK; #1832221, MLK; and #2012670, MLK) with additional support from the US Department of Energy, Office of Biological and Environmental Research Program (DE-SC0021112, MLK). Tyler Messerschmidt and Alex Smith helped with field work. This is contribution 4115 of the Virginia Institute of Marine Science, William & Mary.

Author contributions. Y.C. designed the study, performed the analysis, and wrote the initial draft. M.L.K conceived the idea, contributed to the study design and revised the manuscript. All authors interpreted the data.

Competing interests. The authors declare no competing interests.

Figure Legends/Captions (for main text figures)

Figure 1. Correspondence between Normalized Difference Vegetation Index (NDVI) trend and vegetation shift in the mid-Atlantic coast of North America, a hotspot for accelerated sea-level rise. **a**. Regional NDVI trend between 1984 and 2020 for areas less than 5 m above sea level, generally illustrating wetland browning (orange) and upland greening (green). The elevation data refers to the Coastal National Elevation Database[54]. Black boxes outline three regional subsets for fine-scale demonstration. **b**. Landscape browning associated with coastal forest retreat in Blackwater National Wildlife Refuge (38.4°N, 76.1°W, Maryland); **c**. Landscape browning due to marsh and forest loss at Prime Hook National Wildlife Refuge (38.8°N, 75.3°W, Delaware); **d**. Landscape browning driven by marsh erosion along barrier islands in Virginia Coast Reserve (37.2°N, 75.8°W, Virginia). Maps of landcover change (third row in **b-d**) were computed by differencing the landcover maps in 1984 (first row) and 2020 (second row). “Coastal forest loss” corresponds to areas where upland forest or transition forest were replaced by migrating marsh and open water. “Marsh loss” refers to areas of marsh loss to open water. Scale bars in **b-d** correspond to 4 km. See Extended Data Figures 6-7 and Extended Data Table 1-3 for more information on analysis statistics and landcover classifications. Map created using the Ocean Basemap in ArcGIS (v10.7).

Figure 2. Spatial extent of sea-level rise impacts in coastal ecosystems. **a**. Normalized Difference Vegetation Index (NDVI) trend plotted against elevation gradient, including (grey line) or excluding (black line) land-cover and land-use change associated with human activities (e.g. agriculture, urbanization, deforestation and reforestation, Extended Data Table 1). **b**. Histograms showing range shifts of vegetation from 1984 to 2020 along elevation gradient. From top to bottom: marsh, transition forest and upland forest. Note that the *y* axes of the histograms were not plotted on the same scale. “Count” refers to number of Landsat pixels. All statistics were computed after excluding areas of human land-use and land-use change. The vertical lines correspond to mean elevation of vegetation within 0-5 m above sea level in 1984 (solid) and 2020 (dotted). The red lines represent cumulative number of Landsat pixels along elevation in 1984 (solid) and 2020 (dotted). Elevation data[54] is relative to NAVD88, which approximates mean sea level in the region.

Figure 3. Normalized Difference Vegetation Index (NDVI) trend and the associated aboveground biomass change by vegetation type. **a**. Four-year rolling mean NDVI through time, presented by vegetation type along elevation gradients (panels from left to right: 0-0.7 m, 0.7-1.9 m, and 1.9-5 m above sea level). Solid and dotted lines refer to linear regression showing statistically significant ($P < 0.05$, solid line) and marginally significant ($P < 0.1$, dotted line) trends between 1984 and 2020, respectively. **b**. Overall and vegetation-specific aboveground biomass change from 1984 to 2020, indicating a net increase in coastal aboveground biomass. All results were computed on areas free from human land-use and land-use changes.

Figure 4. Environmental drivers for regional patterns of Normalized Difference Vegetation Index (NDVI) trend. **a**. Relative influence of each environmental driver. FF: flooding frequency; Slope: topographical slope; ΔTAP: change in total annual precipitation between 1984-2020; ΔGDD: change in growing degree day between 1984-2020; MST: maximum summer temperature. **b-g**. Partial-dependency plots illustrating the relationship between NDVI trend and each of the environmental drivers. The *x* axes represent the independent variable, and the *y* axes refer to the effect size that each variable has on the NDVI trend. The shaded areas bounding the mean lines represent 95% confidence interval, and the tick marks indicate the deciles of data distribution. All analyses were performed on areas free from human land-use and land-use changes.

References

1. Crowther, T. W. et al. Quantifying global soil carbon losses in response to warming. *Nature* **540**, 104–108 (2016).
2. Jackson, S. T. Transformational ecology and climate change. *Science* **373**, 1085–1086 (2021).
3. Elmendorf, S. C. et al. Plot-scale evidence of tundra vegetation change and links to recent summer warming. *Nat. Clim. Chang.* **2**, 453–457 (2012).
4. Berner, L. T. et al. Summer warming explains widespread but not uniform greening in the Arctic tundra biome. *Nat. Commun.* **11**, 4621 (2020).
5. Liang, E. et al. Species interactions slow warming-induced upward shifts of treelines on the Tibetan Plateau. *Proc. Natl. Acad. Sci. U. S. A.* **113**, 4380–4385 (2016).
6. Wang, C. P., Huang, M. T. & Zhai, P. M. Change in drought conditions and its impacts on vegetation growth over the Tibetan Plateau. *Adv. Clim. Chang. Res.* (2021) doi:10.1016/j.accre.2021.04.004.
7. Brandt, M. et al. Human population growth offsets climate-driven increase in woody vegetation in sub-Saharan Africa. *Nat. Ecol. Evol.* **1**, 1–6 (2017).
8. Pausata, F. S. R. et al. The Greening of the Sahara: Past Changes and Future Implications. *One Earth* **2**, 235–250 (2020).
9. Nemani, R. R. et al. Climate-driven increases in global terrestrial net primary production from 1982 to 1999. *Science* **300**, 1560–1563 (2003).
10. Chen, C. et al. China and India lead in greening of the world through land-use management. *Nat. Sustain.* **2**, 122–129 (2019).
11. Zhang, Y., Song, C., Band, L. E., Sun, G. & Li, J. Reanalysis of global terrestrial vegetation

trends from MODIS products: Browning or greening? *Remote Sens. Environ.* **191**, 145–155 (2017).

12. Pugh, T. A. M. et al. Role of forest regrowth in global carbon sink dynamics. *Proc. Natl. Acad. Sci.* **116**, 4382–4387 (2019).

13. Xu, L. et al. Changes in global terrestrial live biomass over the 21st century. *Sci. Adv.* **7**, eabe9829 (2021).

14. FitzGerald, D. M., Fenster, M. S., Argow, B. A. & Buynevich, I. V. Coastal Impacts Due to Sea-Level Rise. *Annu. Rev. Earth Planet. Sci.* **36**, 601–647 (2008).

15. Kirwan, M. L. & Gedan, K. B. Sea-level driven land conversion and the formation of ghost forests. *Nat. Clim. Chang.* **9**, 450–457 (2019).

16. Kirwan, M. L. & Megonigal, J. P. Tidal wetland stability in the face of human impacts and sea-level rise. *Nature* **504**, 53–60 (2013).

17. McLeod, E. et al. A blueprint for blue carbon: Toward an improved understanding of the role of vegetated coastal habitats in sequestering CO_2. *Front. Ecol. Environ.* **9**, 552–560 (2011).

18. Macreadie, P. I. et al. The future of Blue Carbon science. *Nat. Commun.* **10**, 3998 (2019).

19. Lovelock, C. E. & Reef, R. Variable Impacts of Climate Change on Blue Carbon. *One Earth* **3**, 195–211 (2020).

20. Schepers, L., Brennand, P., Kirwan, M. L., Guntenspergen, G. R. & Temmerman, S. Coastal Marsh Degradation Into Ponds Induces Irreversible Elevation Loss Relative to Sea Level in a Microtidal System. *Geophys. Res. Lett.* **47**, 1–10 (2020).

21. Törnqvist, T. E., Jankowski, K. L., Li, Y. & González, J. L. Tipping points of Mississippi Delta marshes due to accelerated sea-level rise. *Sci. Adv.* **6**, eaaz5512 (2020).

22. Herbert, E. R., Windham-Myers, L. & Kirwan, M. L. Sea-level rise enhances carbon accumulation in United States tidal wetlands. *One Earth* **4**, 425–433 (2021).

23. Rogers, K. et al. Wetland carbon storage controlled by millennial-scale variation in relative sea-level rise. *Nature* **567**, 91–95 (2019).

24. Wang, F., Lu, X., Sanders, C. J. & Tang, J. Tidal wetland resilience to sea level rise increases their carbon sequestration capacity in United States. *Nat. Commun.* **10**, 5434 (2019).

25. Smith, A. J. & Kirwan, M. L. Sea Level ‐ Driven Marsh Migration Results in Rapid Net Loss of Carbon. *Geophys. Res. Lett.* **48**, 1 ‐ 11 (2021).

26. Smart, L. S. et al. Aboveground carbon loss associated with the spread of ghost forests as sea levels rise. *Environ. Res. Lett.* **15**, (2020).

27. Osland, M. J. et al. Beyond just sea ‐ level rise: considering macroclimatic drivers within coastal wetland vulnerability assessments to climate change. *Glob. Chang. Biol.* **22**, 1 ‐ 11 (2016).

28. Ward, N. D. et al. Representing the function and sensitivity of coastal interfaces in Earth system models. *Nat. Commun.* **11**, 1–14 (2020).

29. Saintilan, N. et al. Thresholds of mangrove survival under rapid sea level rise. *Science* **368**, 1118–1121 (2020).

30. Kirwan, M. L., Guntenspergen, G. R. & Morris, J. T. Latitudinal trends in Spartina alterniflora productivity and the response of coastal marshes to global change. *Glob. Chang. Biol.* **15**, 1982–1989 (2009).

31. Osland, M. J. et al. Climate and plant controls on soil organic matter in coastal wetlands. *Glob. Chang. Biol.* **24**, 5361–5379 (2018).

32. Schieder, N. W., Walters, D. C. & Kirwan, M. L. Massive Upland to Wetland Conversion Compensated for Historical Marsh Loss in Chesapeake Bay, USA. *Estuaries and Coasts* **41**, 940–951 (2018).

33. Schieder, N. W. & Kirwan, M. L. Sea-level driven acceleration in coastal forest retreat. *Geology* **47**, 1151–1155 (2019).

34. Ganju, N. K. et al. Spatially integrative metrics reveal hidden vulnerability of microtidal salt marshes. *Nat. Commun.* **8**, (2017).

35. Jankowski, K. L., Törnqvist, T. E. & Fernandes, A. M. Vulnerability of Louisiana's coastal wetlands to present-day rates of relative sea-level rise. *Nat. Commun.* **8**, 1–7 (2017).

36. Kauffman, J. B. et al. Total ecosystem carbon stocks at the marine-terrestrial interface: Blue carbon of the Pacific Northwest Coast, United States. *Glob. Chang. Biol.* **26**, 5679–5692 (2020).

37. Morris, J. T., Sundareshwar, P. V., Nietch, C. T., Kjerfve, B. & Cahoon, D. R. Responses of coastal wetlands to rising sea level. *Ecology* **83**, 2869–2877 (2002).

38. Kirwan, M. L. & Guntenspergen, G. R. Feedbacks between inundation, root production, and shoot growth in a rapidly submerging brackish marsh. *J. Ecol.* **100**, 764–770 (2012).

39. Kirwan, M. L. & Mudd, S. M. Response of salt-marsh carbon accumulation to climate change. *Nature* **489**, 550–553 (2012).

40. Friess, D. A. et al. The State of the World's Mangrove Forests: Past, Present, and Future. *Annu. Rev. Environ. Resour.* **44**, 89–115 (2019).

41. Hooijer, A. & Vernimmen, R. Global LiDAR land elevation data reveal greatest sea-level rise vulnerability in the tropics. *Nat. Commun.* **12**, 3592 (2021).

42. Więski, K. & Pennings, S. C. Climate Drivers of Spartina alterniflora Saltmarsh Production

in Georgia, USA. *Ecosystems* **17**, 473–484 (2014).

43. Sallenger, A. H., Doran, K. S. & Howd, P. A. Hotspot of accelerated sea-level rise on the Atlantic coast of North America. *Nat. Clim. Chang.* **2**, 884–888 (2012).

44. Ury, E. A., Yang, X., Wright, J. P. & Bernhardt, E. S. Rapid deforestation of a coastal landscape driven by sea - level rise and extreme events. *Ecol. Appl.* **31**, 1 - 11 (2021).

45. Coldren, G. A. et al. Chronic warming stimulates growth of marsh grasses more than mangroves in a coastal wetland ecotone. *Ecology* **97**, 3167–3175 (2016).

46. Chen, Y., Hu, F. S. & Lara, M. J. Divergent shrub-cover responses driven by climate, wildfire, and permafrost interactions in Arctic tundra ecosystems. *Glob. Chang. Biol.* **27**, 652–663 (2021).

47. Kelly, R., Genet, H., McGuire, A. D. & Hu, F. S. Palaeodata-informed modelling of large carbon losses from recent burning of boreal forests. *Nat. Clim. Chang.* **6**, 79–82 (2016).

48. Gabler, C. A. et al. Macroclimatic change expected to transform coastal wetland ecosystems this century. *Nat. Clim. Chang.* **7**, 142–147 (2017).

49. Zhao, M. & Running, S. W. Drought-induced reduction in global terrestrial net primary production from 2000 through 2009. *Science* **329**, 940–943 (2010).

50. Krauss, K. W. et al. The Role of the Upper Tidal Estuary in Wetland Blue Carbon Storage and Flux. *Global Biogeochem. Cycles* **32**, 817–839 (2018).

51. Theuerkauf, E. J., Stephens, J. D., Ridge, J. T., Fodrie, F. J. & Rodriguez, A. B. Carbon export from fringing saltmarsh shoreline erosion overwhelms carbon storage across a critical width threshold. *Estuar. Coast. Shelf Sci.* **164**, 367–378 (2015).

52. White, E. E., Ury, E. A., Bernhardt, E. S. & Yang, X. Climate Change Driving Widespread Loss of Coastal Forested Wetlands Throughout the North American Coastal Plain.

Ecosystems (2021) doi:10.1007/s10021-021-00686-w.

53. Molino, G. D., Carr, J. A., Ganju, N. K. & Kirwan, M. L. Variability in marsh migration potential determined by topographic rather than anthropogenic constraints in the Chesapeake Bay region. *Limnol. Oceanogr. Lett.* (2022). In press.

54. Danielson, J. J., Poppenga, S. K., Tyler, D. J., Palaseanu-Lovejoy, M. & Gesch, D. B. Coastal National Elevation Database. Fact Sheet http://pubs.er.usgs.gov/publication/fs20183037 (2018) doi:10.3133/fs20183037.

METHODS

Regional Setting

We analyzed the response of coastal vegetation to interacting facets of climate change across the U.S. mid-Atlantic coast. The study area encompasses the Delaware Bay and the Chesapeake Bay – the largest coastal-plain estuary in North America. The mid-Atlantic coast is an ideal region for studying the impacts of interacting components of climate change on coastal ecosystems because it represents a known hotspot of relative sea-level rise[43], and rapidly changing precipitation and temperature (Extended Data Figures 1-2). Relative sea-level rise rates are 2-3X faster than the global average, and accelerating towards a modern rate of 4-10 mm yr^{-1} [43]. Coastal ecosystems are particularly vulnerable to sea-level rise in the region because of limited sediment inputs, a microtidal tide range, and a gently sloping coastal plain. Indeed, both extensive marsh loss and forest retreat have been widely observed[15,32,52].

We analyzed 36-year Normalized Difference Vegetation Index (NDVI) trends and mapped landcover changes from 1984 to 2020 for all areas between 0 and 5 m above sea level (Extended Data Figure 1), an elevation range extending from perennially inundated coastal lowlands, through periodically flooded intertidal wetlands, to seldomly flooded uplands that show no sign of seawater intrusion[25,55,56]. The elevation data used to define our study area refers to the digital elevation model (DEM) of the Coastal National Elevation Database (CoNED)[54]. Elevations are relative to the North American Vertical Datum of 1988, which approximates mean sea level in the region.

Data preprocessing and NDVI trend analysis

We acquired all orthorectified, Tier-1 Landsat surface reflectance scenes with cloud cover less than 60% (n = 5,126) by Landsat-5 Thematic Mapper (TM), Landsat-7 Enhanced Thematic Mapper-plus (ETM+) and Landsat-8 Operational Land Imager (OLI)[57] that cover the entire U.S.

mid-Atlantic region between March 24, 1984 and December 29, 2020. All images were processed with the ancillary Quality Assessment bands to mask pixels associated with water, cloud, cloud shadow, snow, ice and sensor-related issues[58] in R (v 4.1.1). The resulting products were further processed to filter pixels of partial inundation using the Tidal Marsh Inundation Index[59,60]. Residual cloud, shadow, haze and smoke were removed by threshold-filtering the blue (surface reflectance > 0.07) and red (surface reflectance < 0.01)[61] spectral bands.

Remotely-sensed NDVI is strongly correlated with growing-season plant biomass and productivity in a myriad of terrestrial and aquatic ecosystems[62–66]. Our study region consists of multiple ecosystems that vary in vegetation phenology. To ensure reliable trend detection across the spatially-complex coastal landscapes, we examined monthly NDVI patterns of different vegetation types (i.e. marsh, transition forest, and upland deciduous and evergreen forest) to identify the best timing for consistent NDVI observations (Extended Data Figure 3)[4]. To achieve that, we randomly selected ~3000 sites for each vegetation across the entire region (Extended Data Figure 3) based on field observations, published study[25,32,33,55,67], the high-resolution National Agriculture Imagery Program (NAIP) aerial imagery, and the Conservation Innovation Center (CIC) landcover map. We extracted the NDVI data sensed by Landsat-7 at each site over the most recent five years (2016-2020). Extended Data Figure 3 indicates the months of peak growing-season in our study region (July-August) when NDVI is maximized and remains relatively stable throughout the time span. This temporal pattern is consistent across vegetation types and from year to year. Therefore, the images acquired annually between July 1st and August 31st were used for the trend analysis.

We validated the correlation between Landsat-derived NDVI and peak growing-season plant biomass across the study region (Extended Data Figure 4) using field measurements of aboveground biomass (AGB) in the U.S. mid-Atlantic coast archived in the Long-term Ecological Research (LTER) Network (Extended Data Figure 1). Specifically, we used datasets related to the biomass of marshes along the York River[68,69] and outer Atlantic Coast[70] of Virginia, and forests distributed throughout the Chesapeake Bay[25,71] and Delaware Bay[72]. Some of the field sites have repeated biomass measurements collected over multiple years and transects. All the measurements were screened for outliers that exceeded site mean by more than 2 standard deviation[70]. For each of the measurements, the corresponding NDVI data was retrieved from Landsat-7 images. Both the biomass measurements and the NDVI data were averaged across year and transect for each study site. Given differences in the size between Landsat pixels and field sites, only ground-based measurements representative of biomass at the 30 × 30 m pixel scale were included. Sites that account only for a fraction of the pixel (e.g. located near creekbanks or farmlands) were discarded after consulting high-resolution drone images and NAIP aerial photos. Eventually, the modeled relationship between NDVI and AGB (n = 125) pooled from all field sites of marsh, transition forest, and upland forest is robust ($P < 0.0001$) with a coefficient of determination (R^2) of 0.72 (Extended Data Figure 4).

Previous studies have revealed that small systematic biases in surface reflectance may exist across Landsat sensors that can lead to an artificial upward trend of NDVI through time[4,61,62,73,74]. Since our study spans 36 years that involves multiple generations of sensors (TM, ETM+, and OLI), we systematically evaluated NDVI data derived from Landsat-5, 7 and 8 in the region to constrain potential errors introduced by sensor difference (Extended Data Figure 5). The operation timeline of Landsat-7 overlaps with Landsat-5 during 1999-2011, and with Landsat-8 during 2013-present[57]. Therefore, we took advantage of the overlapping scenes collected by concurrent sensors to cross-validate NDVI of Landsat-5 and Landsat-8 against that of Landsat-7, similar to the methodology described by refs.[4,73] (Extended Data Figure 5). We randomly selected 35 pairs of cloud-free Landsat-5 and Landsat-7 images, and 43 pairs of Landsat-8 and Landsat-7 images from ten and eight overlapping summers, respectively. The paired NDVI data were extracted every 600 m (20 pixels) apart across all overlapping areas, and the data were analyzed with linear regression. Our results agree with earlier work suggesting differences in NDVI between sensors (Extended Data Figure 5), and all Landsat-5 and Landsat-8 derived NDVI was adjusted to Landsat-7 according to the linear equations presented in Extended Data Figure 5.

The processed NDVI data were then stacked in time series from 1984 to 2020 for trend analysis with the non-parametric Theil-Sen slope estimator[75], a widely used approach for quantifying monotonic trends with the advantage of being insensitive to outliers[76]. The significance of the NDVI trends was tested with the rank-based Mann-Kendall test[75], and trends were considered statistically significant at the level of $\alpha < 0.1$ [4,10] (Extended Data Figure 6, 61.4% of the pixels tested significant). All statistics were conducted in R (v 4.1.1) using the *zyp* package[75]. NDVI at the beginning (1984) and the end (2020) of the study period were computed for each pixel, and the resulting dataset was then converted to AGB according to the NDVI-AGB relationship (Extended Data Figure 4). The cumulative AGB change from 1984 to 2020 was then estimated as the difference between AGB in 2020 and 1984. For pixels where no significant NDVI trends were detected ($P \geq 0.1$), the cumulative AGB change was assigned to 0.

Landcover mapping and validation

We generated two regional landcover maps (30 by 30 m) with seven classes (Marsh, Transition Forest, Upland Forest, Water, Sandbar, Agriculture and Urban Area, Extended Data Table. 1), one in 1984 and one in 2020 using the random forest (RF) algorithm[77] implemented in R (v 4.1.1, packages of *caret* and *randomForest*) (Extended Data Figure 7). For each mapping, we acquired

Landsat images during multiple seasons corresponding to distinct plant phenological phases[78,79]: the greening/leaf-out season (March-April), the peak growing-season (July-August), and the senescent/leaf-off season (October-November) for enhanced separability between spectrally-similar classes (Extended Data Figure 3). The input predictors comprise layers of individual Landsat spectral bands, Landsat-derived multispectral indices, and biophysical metrics computed from the 1 m CoNED DEM (Extended Data Table. 2). The biophysical metrics were resampled to 30 m resolution using bilinear interpolation. All input layers were then aligned to identical pixel centers and projected to a common geographic coordinate system before classification in R (v 4.1.1).

The training and validation sites for the 2020 and 1984 mapping were identified according to high-resolution contemporary (2018-2020) and historical (1982-1986) images, respectively. To ensure that the sites sampled cover all landcover types with relatively even distribution between classes, we initially selected the sites via stratified random sampling (strata = landcover type) from the most recent CIC map in 2013 (for the 2020 landcover mapping) and the earliest NOAA Coastal Change Analysis Program (C-CAP) map in 1996 (for the 1984 landcover mapping)[56]. In brief, we randomly sampled ~5,000 sites for each landcover type except for Transition Forest based on the two preexisting maps. Sites in the same class were picked across the entire region with a minimum distance of 1 km apart from one another. The classification of each site was examined for accuracy and corrected if mis-labeled according to high-resolution satellite/aerial images archived in Google Earth Engine[80] or downloaded from the USGS (https://earthexplorer.usgs.gov/). Since transition forest has not been mapped in previous efforts, all sites of this class were visually identified (n = 5,000) according to published delineation[25,32,33,55,67], field observations, and contemporary and historical images across the region, similarly with a between-site distance ≥1 km. We then randomly divided the sites of each class into the training and validation groups in the ratio of 60% to 40% (Extended Data Figure 7).

We ran the RF classifier on all training sites and eliminated insignificant factors in a backward fashion to optimize model fitting[79,81] (Extended Data Figure 7). The most parsimonious models reaching an overall classification accuracy around 90% were used for producing the regional maps (Extended Data Table. 2). We then applied four steps of post-processing to refine the maps for enhanced accuracy. First, we excluded degrading forests classified as Transition Forest but attributable to factors other than seawater intrusion (e.g. insect outbreak, over-herbivory, and pollution[82]). These misclassified Transition Forests were identified using the combination of flooding frequency = 0% (Global Surface Water dataset[83]) and elevation > 2.5 m above sea level (> upper tidal range). Second, marshes in areas with flooding frequency > 95% were assigned to water[84] according to the Global Surface Water dataset[83]. Third, additional areas identified by the Global Forest Cover Change database[85] as newly lost or gained (deforestation and reforestation) were excluded from Upland Forest in 2020 (Extended Data Table. 1). All the above processes were visually verified by high-resolution images. Last, areas that were masked from auto-classification by image preprocessing (e.g. contaminated by cloud and cloud shadow, ~5% of all area) were manually classified by digitizing high-resolution images, following the same approach of ref.[33]. The final 1984 and 2020 landcover maps were validated extensively across the region with validation sites, which attained an overall classification accuracy of 91.0% and 93.1%, respectively (Extended Data Table 3).

Analysis for environmental drivers

We analyzed the environmental drivers of NDVI trend and their relative influence (%) using a boosted regression tree (BRT) model[86] (packages of *dismo* and *gbm* in R v 4.1.1) in all areas free from human impacts as identified by our landcover maps (Extended Data Table. 1). The BRT model was chosen for its superiority in handling high-order interactions and collinearity of covariates, as well as the sophistication in managing missing data and outliers[86,87]. We identified candidate predictors according to previous study on coastal vegetation change and carbon cycling[27,31,33,38,48,88–90], which can be broadly categorized into climatological-related variables and sea-level-related variables.

The climate data (temperature, precipitation, and vapor pressure deficit) for the BRT model were derived from the PRISM Climate Group (daily dataset between 1984 and 2020 with spatial resolution of 800 m)[91]. The annual growing degree days (GDD) was calculated from the temperature data as the number of days when daily average is greater or equal to 10 ºC [30,88]. Aside from the analysis-ready 30-year normals[91], the input climate variables also include the change (Δ) of temperature, precipitation and GDD from 1984 to 2020, computed as the product between the slope simulated by the Theil-Sen slope estimator[75] using annual inputs, and the number of years during the period (36 years). The sea-level related datasets were downloaded directly from the Global Surface Water dataset (three variables: flooding frequency, flooding seasonality and flooding change intensify; 30 m resolution datasets generated between 1984-2020)[83] or computed from the CoNED DEM (four variables: elevation, topographic slope, aspect and topographic position index[92]; static 1 m resolution dataset). All datasets were projected to a common geographic coordinate system and resampled to the same spatial resolution (800 m) by bilinear interpolation before analysis.

We initiated the BRT model with all candidate predictors, and removed uninfluential, cross-dependent/cross-correlative variables step by step until achieving a single reduced model that contains only significant variables with relative influence greater than 5% [93]. The default ten-fold cross-validation was used to optimize model performance. The final model was fitted with a tree complexity of 10, learning rate of 0.0005 and bag fraction (stochasticity) of 0.75 that result in > 5,000 trees.

Data Availability. All Landsat Level-1 surface reflectance images are publicly available from the USGS EarthExplorer (https://earthexplorer.usgs.gov/) or via Google Cloud Landsat dataset (https://cloud.google.com/storage/docs/public-datasets/landsat). All field-based biomass data are detailed in ref.[25,68-72] and available in the Virginia Coast Reserve Long-Term Ecological Research repository (http://www.vcrlter.virginia.edu/cgi-bin/browseData.cgi). The landcover maps and the NDVI trend map are publicly available at the Environmental Data Initiative Data Repository (https://doi.org/10.6073/pasta/4ae5ac3fbdb6a20dcdcb2ff36487d292).

Code Availability. The study does not report original code. All code used this study is available from the corresponding author upon reasonable request.

Methods-only references

55. Molino, G. D., Defne, Z., Aretxabaleta, A. L., Ganju, N. K. & Carr, J. A. Quantifying Slopes as a Driver of Forest to Marsh Conversion Using Geospatial Techniques: Application to Chesapeake Bay Coastal-Plain, United States. *Front. Environ. Sci.* **9**, (2021).

56. NOAA Office for Coastal Management. NOAA Coastal Change Analysis Program (C-CAP) Regional Land Cover Database. Data collected 1995-present. Charleston, SC. https://coast.noaa.gov/digitalcoast/tools/lca.html (2016).

57. Woodcock, C. E. et al. Free Access to Landsat Imagery. *Science* **320**, 1011a-1011a (2008).

58. Sayler, K. & Zanter, K. Earth Resources Observation and Science (EROS) Center Science Processing Architecture (ESPA) On-Demand Interface User Guide. Version 4.0. (2020).

59. O'Connell, J. L., Mishra, D. R., Cotten, D. L., Wang, L. & Alber, M. The Tidal Marsh Inundation Index (TMII): An inundation filter to flag flooded pixels and improve MODIS tidal marsh vegetation time-series analysis. *Remote Sens. Environ.* **201**, 34–46 (2017).

60. Campbell, A. D. & Wang, Y. Salt marsh monitoring along the mid-Atlantic coast by Google Earth Engine enabled time series. *PLoS One* **15**, e0229605 (2020).

61. Ju, J. & Masek, J. G. The vegetation greenness trend in Canada and US Alaska from 1984-2012 Landsat data. *Remote Sens. Environ.* **176**, 1–16 (2016).

62. Berner, L. T., Jantz, P., Tape, K. D. & Goetz, S. J. Tundra plant above-ground biomass and shrub dominance mapped across the North Slope of Alaska. *Environ. Res. Lett.* **13**, (2018).

63. Myers-Smith, I. H. et al. Complexity revealed in the greening of the Arctic. *Nat. Clim. Chang.* **10**, 106–117 (2020).

64. Beck, P. S. A. et al. Changes in forest productivity across Alaska consistent with biome shift. *Ecol. Lett.* **14**, 373–379 (2011).

65. Zoffoli, M. L. et al. Sentinel-2 remote sensing of Zostera noltei-dominated intertidal seagrass meadows. *Remote Sens. Environ.* **251**, 112020 (2020).

66. Byrd, K. B. et al. A remote sensing-based model of tidal marsh aboveground carbon stocks for the conterminous United States. *ISPRS J. Photogramm. Remote Sens.* **139**, 255–271 (2018).

67. White, E. & Kaplan, D. Identifying the effects of chronic saltwater intrusion in coastal floodplain swamps using remote sensing. *Remote Sens. Environ.* **258**, 112385 (2021).

68. Gillen, M. N., Messerschmidt, T. C. & Kirwan, M. L. Biophysical controls of marsh soil shear strength along an estuarine salinity gradient. *Earth Surf. Dyn.* **9**, 413–421 (2021).

69. Gillen, M., Messerschmidt, T. & Kirwan, M. Shear Stress, Biomass, Bulk Density, Organic Matter on the Bank of the York River, VA. *Environ. Data Initiat.* (2021).

70. Kirwan, M. L., Christian, R. R., Blum, L. K. & Brinson, M. M. On the Relationship Between Sea Level and Spartina alterniflora Production. *Ecosystems* **15**, 140–147 (2012).

71. Smith, A., Kirwan, M. & Messerschmidt, T. Carbon stocks in forests transitioning to salt marsh at four sites in the Chesapeake Bay region, 2019. *Environ. Data Initiat.* (2021).

72. Chen, Y., Messerschmidt, T., Smith, A. & Kirwan, M. Coastal Forest Aboveground Biomass Data at six sites in the Chesapeake Bay and Delaware Bay region, 2021. *Environ. Data Initiat.* (2022).

73. Roy, D. P. et al. Characterization of Landsat-7 to Landsat-8 reflective wavelength and normalized difference vegetation index continuity. *Remote Sens. Environ.* **185**, 57–70 (2016).

74. Claverie, M., Vermote, E. F., Franch, B. & Masek, J. G. Evaluation of the Landsat-5 TM and Landsat-7 ETM+ surface reflectance products. *Remote Sens. Environ.* **169**, 390–403

(2015).

75. Bronaugh, D. & Werner, A. zyp: Zhang + Yue-Pilon Trends Package Version 0.10-1.1. https://cran.r-project.org/web/packages/zyp/index.html (2019).

76. Wilcox, R. R. Fundamentals of Modern Statistical Methods: Substantially Improving Power and Accuracy, 2nd edition. (Springer, 2011).

77. Breiman, L. Random Forests. *Mach. Learn.* **45**, 5–32 (2001).

78. Tian, J. et al. Development of spectral-phenological features for deep learning to understand Spartina alterniflora invasion. *Remote Sens. Environ.* **242**, 111745 (2020).

79. Zhang, F. & Yang, X. Improving land cover classification in an urbanized coastal area by random forests: The role of variable selection. *Remote Sens. Environ.* **251**, 112105 (2020).

80. Gorelick, N. et al. Google Earth Engine: Planetary-scale geospatial analysis for everyone. *Remote Sens. Environ.* **202**, 18–27 (2017).

81. Liaw, A. & Wiener, M. Classification and Regression by randomForest. *R News* **2**, 18–22 (2002).

82. van Lierop, P., Lindquist, E., Sathyapala, S. & Franceschini, G. Global forest area disturbance from fire, insect pests, diseases and severe weather events. *For. Ecol. Manage.* **352**, 78–88 (2015).

83. Pekel, J.-F., Cottam, A., Gorelick, N. & Belward, A. S. High-resolution mapping of global surface water and its long-term changes. *Nature* **540**, 418–422 (2016).

84. Wang, X. et al. Tracking annual changes of coastal tidal flats in China during 1986–2016 through analyses of Landsat images with Google Earth Engine. *Remote Sens. Environ.* **238**, (2020).

85. Hansen, M. C. et al. High-Resolution Global Maps of 21st-Century Forest Cover Change.

Science **342**, 850–853 (2013).

86. Elith, J., Leathwick, J. R. & Hastie, T. A working guide to boosted regression trees. *J. Anim. Ecol.* **77**, 802–813 (2008).

87. La Marca, W. et al. The influence of data source and species distribution modelling method on spatial conservation priorities. *Divers. Distrib.* **25**, 1060–1073 (2019).

88. Liu, W. et al. Climate and geographic adaptation drive latitudinal clines in biomass of a widespread saltmarsh plant in its native and introduced ranges. *Limnol. Oceanogr.* **65**, 1399–1409 (2020).

89. Wiberg, P. L., Fagherazzi, S. & Kirwan, M. L. Improving Predictions of Salt Marsh Evolution Through Better Integration of Data and Models. *Ann. Rev. Mar. Sci.* **12**, 389–413 (2020).

90. Coldren, G. A., Langley, J. A., Feller, I. C. & Chapman, S. K. Warming accelerates mangrove expansion and surface elevation gain in a subtropical wetland. *J. Ecol.* **107**, 79–90 (2019).

91. PRISM Climate Group. Oregon State Univ. (2020).

92. Vinod, P. G. Development of topographic position index based on Jenness algorithm for precision agriculture at Kerala, India. *Spat. Inf. Res.* **25**, 381–388 (2017).

93. Chen, Y., Lara, M. J., Jones, B. M., Frost, G. V. & Hu, F. S. Thermokarst acceleration in Arctic tundra driven by climate change and fire disturbance. *One Earth* **4**, 1718–1729 (2021).

94. Wickham, J., Stehman, S. V., Sorenson, D. G., Gass, L. & Dewitz, J. A. Thematic accuracy assessment of the NLCD 2016 land cover for the conterminous United States. *Remote Sens. Environ.* **257**, 112357 (2021).

95. Thomas, V. A. et al. Mapping thins to identify active forest management in southern pine plantations using Landsat time series stacks. *Remote Sens. Environ.* **252**, 112127 (2021).

96. Chen, Y. & Kirwan, M. A phenology- and trend-based approach for accurate mapping of sea-level driven coastal forest retreat. *Remote Sens. Environ.* (2022). In press.

97. Gong, P. et al. Stable classification with limited sample: transferring a 30-m resolution sample set collected in 2015 to mapping 10-m resolution global land cover in 2017. *Sci. Bull.* **64**, 370–373 (2019).

98. Carlson, T. N. & Ripley, D. A. On the relation between NDVI, fractional vegetation cover, and leaf area index. *Remote Sens. Environ.* **62**, 241–252 (1997).

99. Diao, C. & Wang, L. Incorporating plant phenological trajectory in exotic saltcedar detection with monthly time series of Landsat imagery. *Remote Sens. Environ.* **182**, 60–71 (2016).

100. Diao, C. & Wang, L. Landsat time series-based multiyear spectral angle clustering (MSAC) model to monitor the inter-annual leaf senescence of exotic saltcedar. *Remote Sens. Environ.* **209**, 581–593 (2018).

101. Guo, B. et al. Dynamic monitoring of soil salinization in Yellow River Delta utilizing MSAVI–SI feature space models with Landsat images. *Environ. Earth Sci.* **78**, 308 (2019).

102. Gitelson, A. A. & Merzlyak, M. N. Remote sensing of chlorophyll concentration in higher plant leaves. *Adv. Sp. Res.* **22**, 689–692 (1998).

103. Huete, A., Justice, C. & Liu, H. Development of vegetation and soil indices for MODIS-EOS. *Remote Sens. Environ.* **49**, 224–234 (1994).

104. Huete, A. . A soil-adjusted vegetation index (SAVI). *Remote Sens. Environ.* **25**, 295–309 (1988).

105. Qi, J., Chehbouni, A., Huete, A. R., Kerr, Y. H. & Sorooshian, S. A modified soil adjusted vegetation index. *Remote Sens. Environ.* **48**, 119–126 (1994).

106. McFEETERS, S. K. The use of the Normalized Difference Water Index (NDWI) in the delineation of open water features. *Int. J. Remote Sens.* **17**, 1425–1432 (1996).

107. Xu, H. Modification of normalised difference water index (NDWI) to enhance open water features in remotely sensed imagery. *Int. J. Remote Sens.* **27**, 3025–3033 (2006).

108. Crist, E. P. & Cicone, R. C. A Physically-Based Transformation of Thematic Mapper Data---The TM Tasseled Cap. *IEEE Trans. Geosci. Remote Sens.* **GE-22**, 256–263 (1984).

109. Baig, M. H. A., Zhang, L., Shuai, T. & Tong, Q. Derivation of a tasselled cap transformation based on Landsat 8 at-satellite reflectance. *Remote Sens. Lett.* **5**, 423–431 (2014).

110. Gislason, P. O., Benediktsson, J. A. & Sveinsson, J. R. Random Forests for land cover classification. *Pattern Recognit. Lett.* **27**, 294–300 (2006).

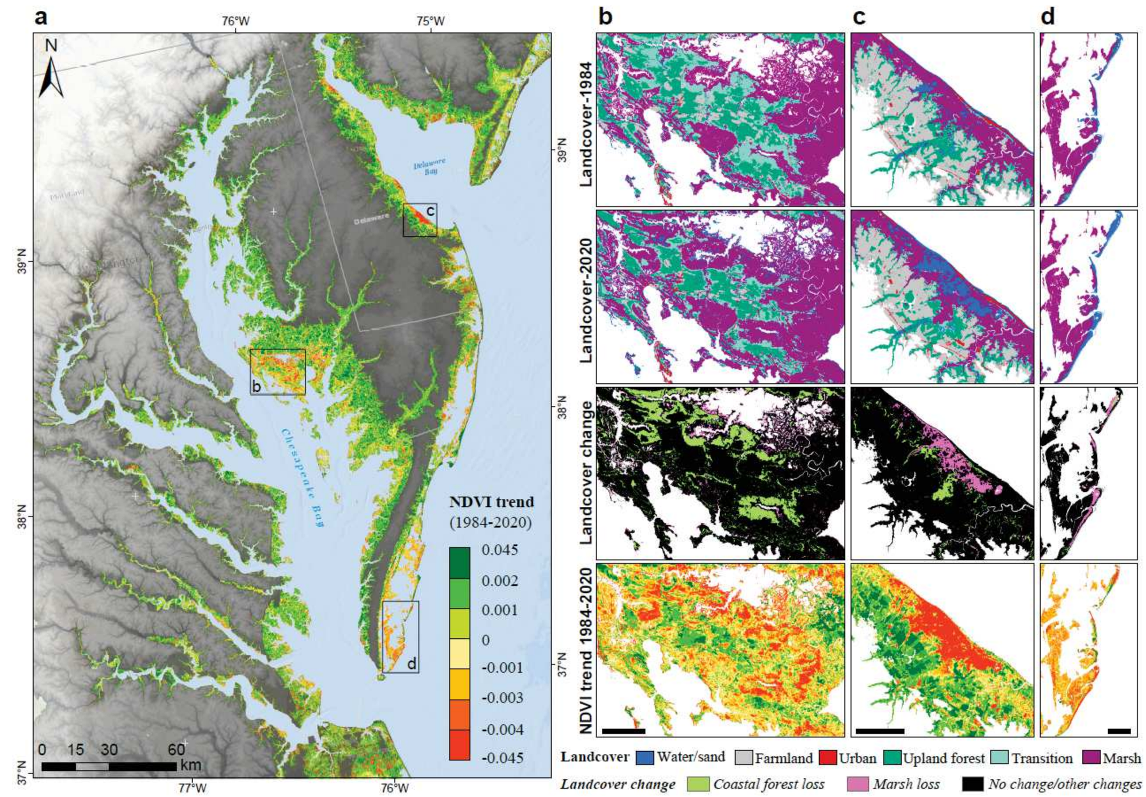

Figure 1. Correspondence between NDVI trend and vegetation shift in the mid-Atlantic coast of North America, a hotspot for accelerated SLR. **a**. Regional NDVI trend between 1984 and 2020 for areas less than 5 m above sea level, generally illustrating wetland browning (orange) and upland greening (green). Black boxes outline three regional subsets for fine-scale demonstration. **b**. Landscape browning associated with coastal forest retreat in Blackwater National Wildlife Refuge (38.4ºN, 76.1ºW, Maryland); **c**. Landscape browning due to marsh and forest loss at Prime Hook National Wildlife Refuge (38.8ºN, 75.3ºW, Delaware); **d**. Landscape browning driven by marsh erosion along barrier islands in Virginia Coast Reserve (37.2ºN, 75.8ºW, Virginia). Maps of landcover change (third row in **b-d**) were computed by differencing the landcover maps in 1984 (first row) and 2020 (second row). “Coastal forest loss” corresponds to areas where upland forest or transition forest were replaced by migrating marsh and open water. “Marsh loss” refers to areas of marsh loss to open water. Scale bars in **b-d** correspond to 4 km. See Extended Data Fig. 6 and Extended Data Table 1-3 for more information on analysis statistics and landcover classifications.

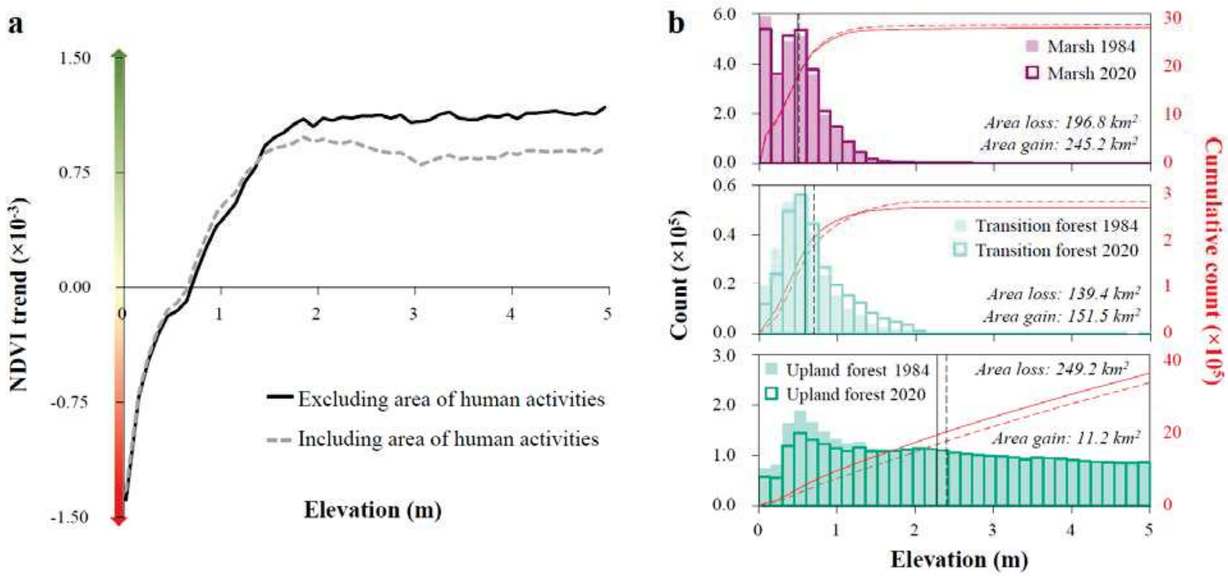

Figure 2. Spatial extent of sea-level rise impacts in coastal ecosystems. **a**. NDVI trend plotted against elevation gradient, including (grey line) or excluding (black line) land-cover and land-use change associated with human activities (e.g. agriculture, urbanization, deforestation and reforestation, Extended Data Table 1). **b**. Histograms showing range shifts of vegetation from 1984 to 2020 along elevation gradient. From top to bottom: marsh, transition forest and upland forest. Note that the *y* axes of the histograms were not plotted on the same scale. "Count" refers to number of Landsat pixels. All statistics were computed after excluding areas of human land-use and land-use change. The vertical lines correspond to mean elevation of vegetation within 0-5 m above sea level in 1984 (solid) and 2020 (dotted). The red lines represent cumulative number of Landsat pixels along elevation in 1984 (solid) and 2020 (dotted). Elevation data[54] is relative to NAVD88, which approximates mean sea level in the region.

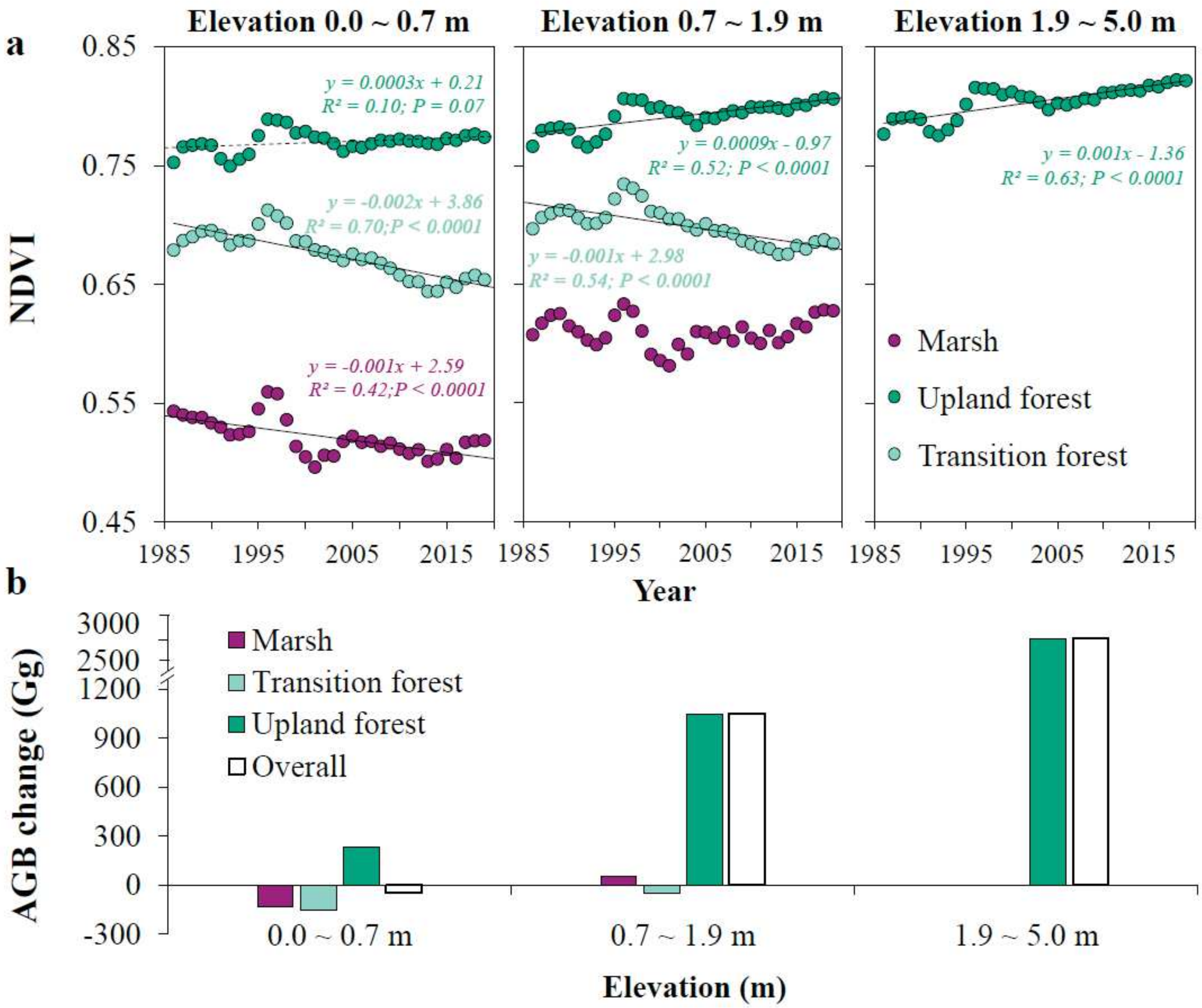

Figure 3. NDVI trend and the associated aboveground biomass change by vegetation type. **a**. Four-year rolling mean NDVI through time, presented by vegetation type along elevation gradients (panels from left to right: 0-0.7 m, 0.7-1.9 m, and 1.9-5 m above sea level). Solid and dotted lines refer to linear regression showing statistically significant (P < 0.05, solid line) and marginally significant (P < 0.1, dotted line) trends between 1984 and 2020, respectively. **b**. Overall and vegetation-specific aboveground biomass change from 1984 to 2020, indicating a net increase in coastal aboveground biomass. All results were computed on areas free from human land-use and land-use changes.

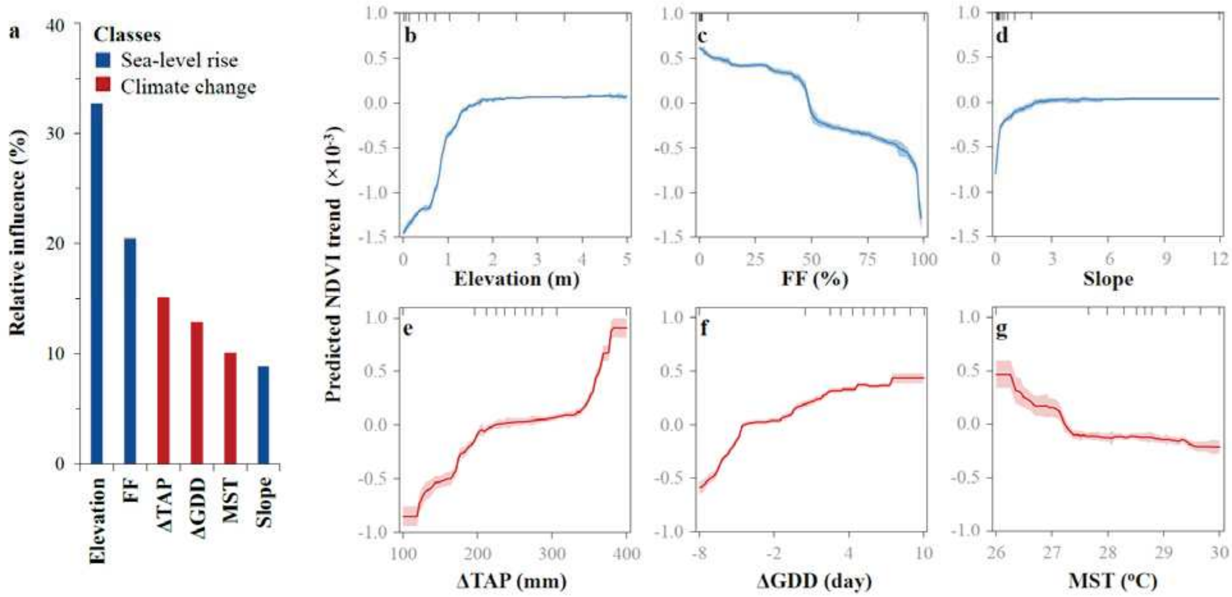

Figure 4. Environmental drivers for regional patterns of NDVI trend. **a**. Relative influence of each environmental driver. FF: flooding frequency; Slope: topographical slope; ΔTAP: change in total annual precipitation between 1984-2020; ΔGDD: change in growing degree day between 1984-2020; MST: maximum summer temperature. **b-g**. Partial-dependency plots illustrating the relationship between NDVI trend and each of the environmental drivers. The *x* axes represent the independent variable, and the *y* axes refer to the effect size that each variable has on the NDVI trend. The shaded areas represent 95% confidence interval, and the tick marks indicate the deciles of data distribution. All analyses were performed on areas free from human land-use and land-use changes.

Extended Data

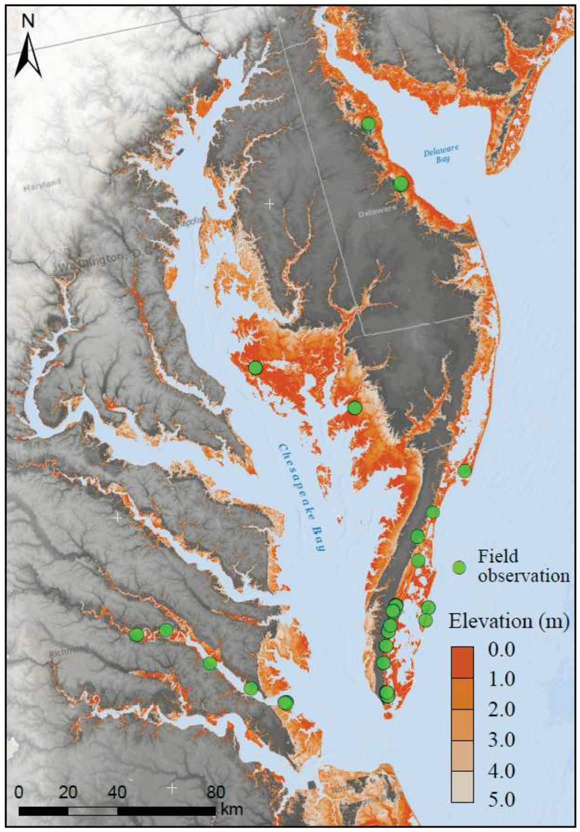

Extended Data Fig. 1. Map of the U.S. mid-Atlantic study region. Green circles denote field sites of aboveground biomass observations. The elevation map refers to the CoNED DEM[54].

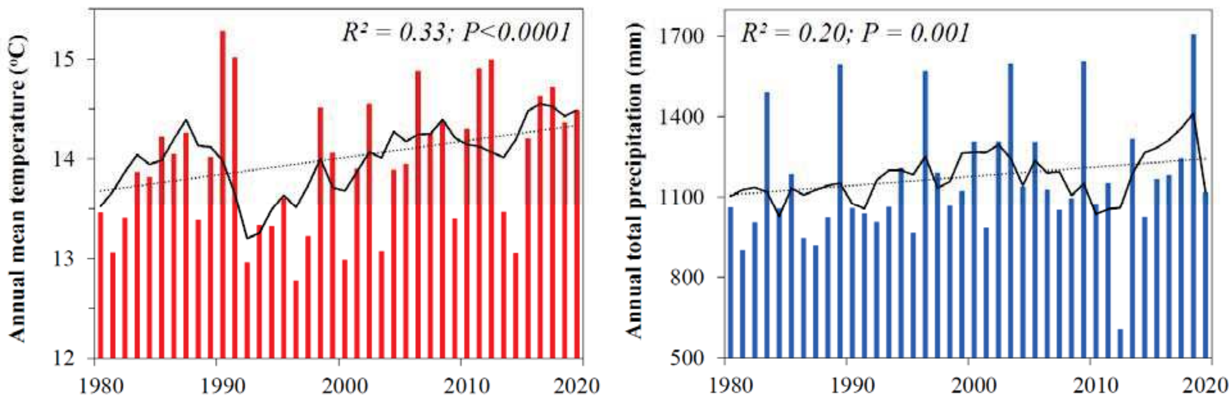

Extended Data Fig. 2. Climate change observed in the study region. The vertical bars represent annual mean temperature (left) and annual total precipitation (right), recorded in the nearest NOAA station in Dover, Delaware. The black lines refer to the 5-yr moving average. The dotted lines represent linear regression that show significant upward trend of long-term temperature and precipitation from 1980 onward. The observed climate data was used for illustrative purposes only. The climate inputs for our boosted regression tree analysis refers to the spatially explicit PRISM datasets.

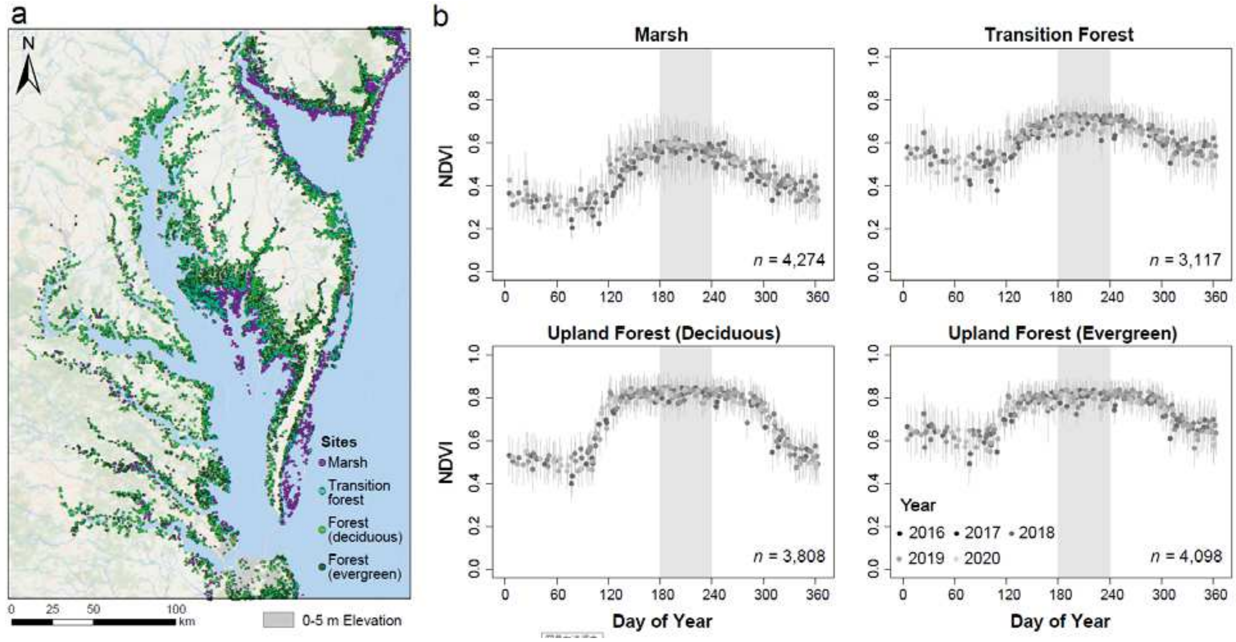

Extended Data Fig. 3. Identifying timing for NDVI trend analysis. **a**. Sites selected randomly for evaluating monthly NDVI patterns. **b**. Monthly NDVI pattern of each vegetation type for the most recent five years. The shaded areas indicate peak growing season when NDVI is maximized and stays relatively consistent. All data are shown as mean ± 1 standard deviation.

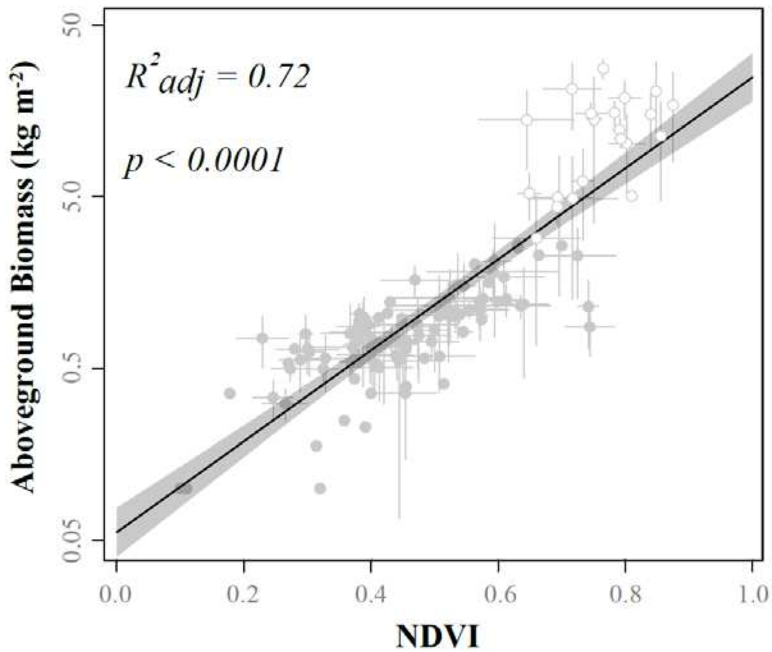

Extended Data Fig. 4. Relationship between peak growing-season NDVI and aboveground biomass. The solid and open symbols correspond respectively to marsh and forest. All biomass data were accessed from the LTER database indicated in Extended Data Fig. 1. The *y*-axis is plotted on a logarithmic scale. The regression function is (aboveground biomass) = $0.05 \times e^{6.02 \times (NDVI)}$, ($P < 0.0001$, F-statistic = 378.5, and RMSE = 0.5766). The uncertainties (grey lines) refer to standard deviations, and the shaded area represents 95% confidence intervals.

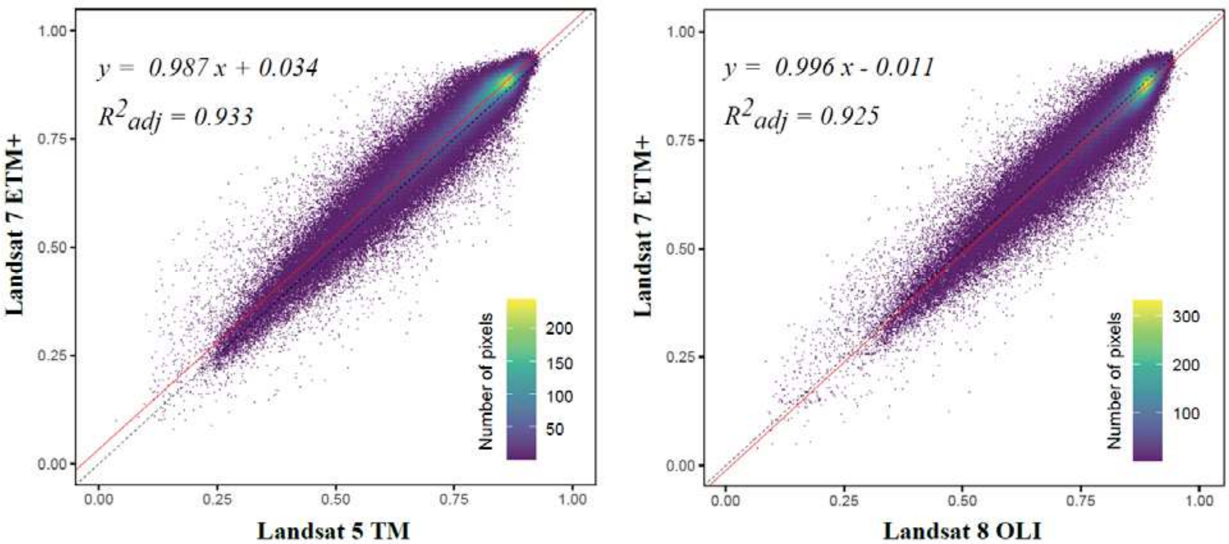

Extended Data Fig. 5. Cross-comparison of NDVI between Landsat sensors. Scatterplots of NDVI by Landsat-5 TM (left) and by Landsat-8 OLI (right) were plotted against NDVI by Landsat-7 ETM+. The solid lines refer to linear regression and dotted lines represent the 1:1 Line superimposed for reference.

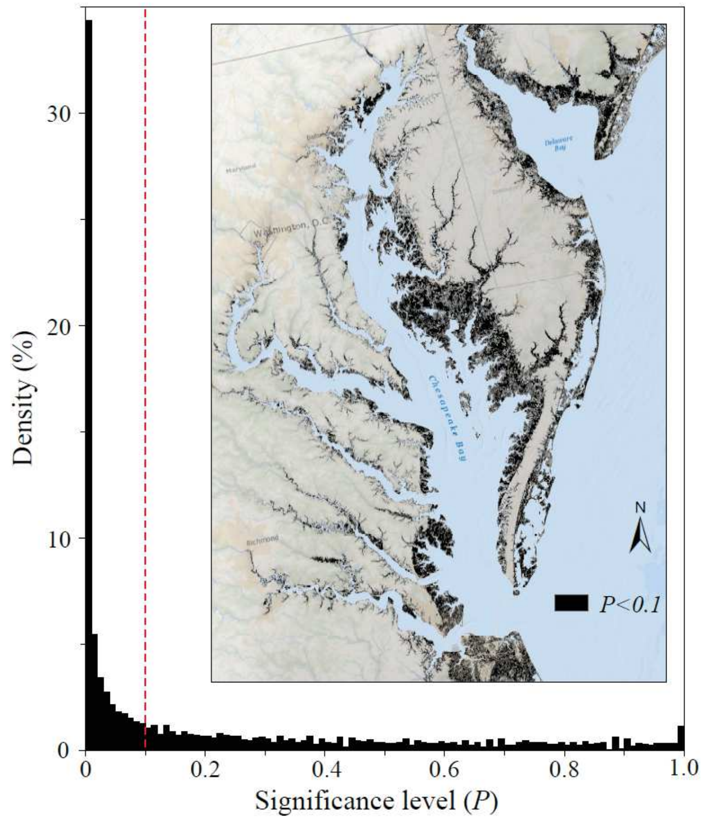

Extended Data Fig. 6. Mann-Kendall test for significant NDVI trends (P < 0.1) in the study region. The inserted map shows all areas that demonstrate statistically significant increases or decreases in NDVI during 1984 to 2020. The density plot summarizes distribution pattern of statistical results among all pixels, and the significance level at P = 0.1 is indicated by the dotted red line.

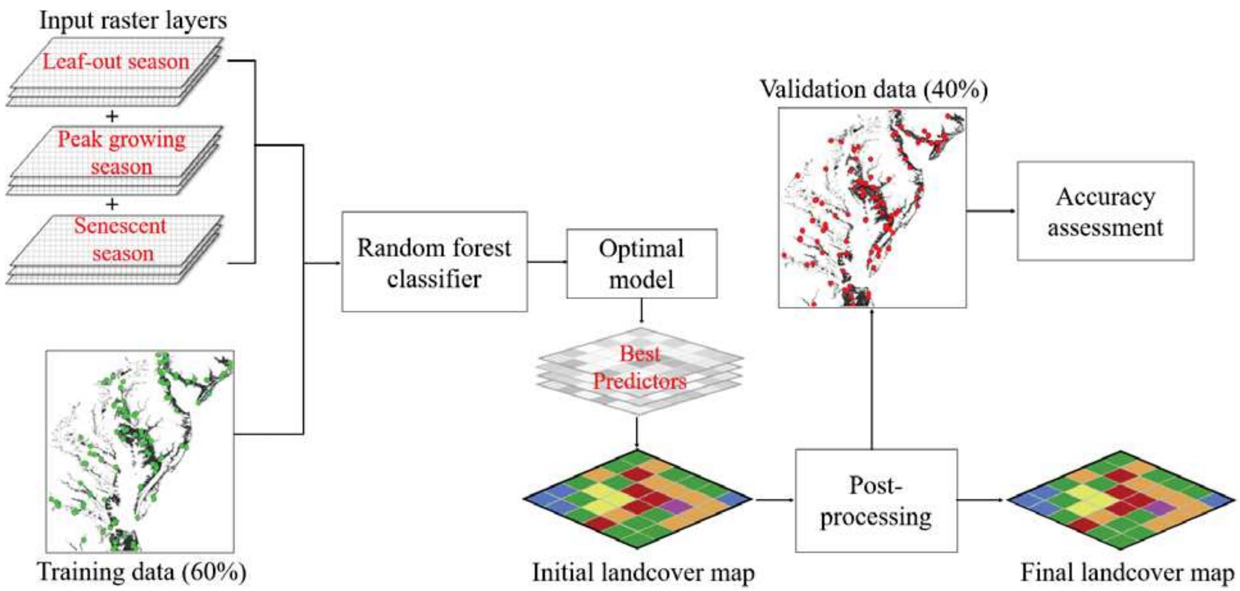

Extended Data Fig. 7. Flowchart for landcover mapping and validation.

Extended Data Table 1. Landcover classes and their definitions used in this study.

Categories	Classes	Definition
Natural habitats	Marsh	Tidal and nontidal wetlands dominated by herbaceous hydrophytes like cordgrass, rushes, and sedges (NOAA C-CAP program[56]).
	Transition forest	Low-lying forests between marsh and upland forests where mortality due to seawater intrusion has already begun. Also known as ghost forests[15,25,26,67], usually with shrubs and marshes present in understory.
	Upland forest	Primary or long-standing secondary forests characterized by closed canopy and mature trees of height greater than 5 m (NOAA C-CAP program[56]).
Human-influenced areas	Agriculture	Managed lands including actively cultivated, fallow or recently abandoned croplands; nursery and plantation for flowers, fruits and other economic plants; managed grasslands and pastures like golf course and residential lawns (National Land Cover Database[94]); and selectively thinned or clear-cut forests (Global Forest Cover Change database[85]).
	Urban area	Developed lands dominated by impervious surface such as asphaltic roads and concrete constructions for residential, institutional, and commercial activities.
Water		Open water with 25% or less of vegetation and soil cover (National Land Cover Database[94]).
Sandbar		Barren, unconsolidated sandy/silty shores, and sparsely vegetated sand dunes subject to constant tidal-driven erosion and redistribution (NOAA C-CAP program[56]).

Extended Data Table 2. Input datasets for random forest classifier. All Landsat images used for landcover mapping were acquired during low tides with cloud cover less than 5%. Predictors in bold are those retained in the final models. “References” refers to studies upon which the selection of candidate predictors is based in this study.

Categories	Predictors*	Data sources	Timing of acquisition	References
Spectral bands	**Blue** **Green** **Red** **NIR** **SWIR1** **SWIR2**	All surface reflectance bands of Landsat-5 for the 1984 mapping; and all surface reflectance bands of Landsat-8 for the 2020 mapping.	Greening/leaf-out season; Peak growing-season; Senescent/leaf-off season.	Refs.[78,79,95–97]
Multispectral indices	NDVI[98] GNDVI[102] **EVI**[103] SAVI[104] **MSAVI**[105] NDWI[106] **mNDWI**[107] **TCP - brightness**[108,109] **TCP - greenness**[108,109] TCP - wetness[108,109]	Computed from surface reflectance bands of Landsat-5 for the 1984 mapping, and from surface reflectance bands of Landsat-8 for the 2020 mapping.	Greening/leaf-out season; Peak growing-season; Senescent/leaf-off season.	Refs.[67,78,95,99–101]
Biophysical attributes	Elevation Slope Aspect TPI[92]	Computed from the 1 m CoNED DEM, resampled to 30m using bilinear interpolation.	Static	Refs.[79,96,110]

* NIR: Near-Infrared; SWIR: Short-wave Infrared; NDVI: Normalized Difference Vegetation Index; GNDVI: Green NDVI; EVI: Enhanced Vegetation Index; SAVI: Soil-Adjusted Vegetation Index; MSAVI: Modified SAVI; NDWI: Normalized Difference Water Index; mNDWI: modified NDWI; TCP: Tasseled Cap Transformation; TPI: Topographical Position Index.

Extended Data Table 3. Classification accuracy of landcover maps.

Classes	1984 landcover map			2020 landcover map		
	Validation (# sites)	*User's* accuracy	*Producer's* accuracy	Validation (# sites)	*User's* accuracy	*Producer's* accuracy
Marsh	2094	91.07%	90.77%	2394	94.32%	90.87%
Transition forest	1904	92.17%	87.44%	2187	93.87%	92.77%
Upland forest	2269	90.17%	94.29%	1975	96.05%	95.95%
Agriculture	2004	91.72%	90.41%	1938	91.64%	95.38%
Urban	1548	96.06%	93.52%	1501	93.27%	91.98%
Water	1799	88.27%	91.06%	2127	90.69%	92.96%
Sandbar	1264	87.66%	89.57%	1463	90.91%	91.66%
Overall accuracy		91.05%			93.10%	